

Femtosecond soft X-ray absorption spectroscopy of warm dense matter at the PAL-XFEL

Jong-Won Lee,^{a,b} Gyeongbo Kang,^{a,b} Minju Kim,^a Minseok Kim,^c Sang Han Park,^c Soonnam Kwon,^c Seonghyeok Yang^{a,b} and Byoung Ick Cho^{a,b*}

^aDepartment of Physics and Photon Science, GIST, Gwangju 61005, Republic of Korea, ^bCenter for Relativistic Laser Science, Institute for Basic Science (IBS), Gwangju 61005, Republic of Korea, and ^cPohang Accelerator Laboratory, Pohang, Gyeongbuk 37673, Republic of Korea. *Correspondence e-mail: bicho@gist.ac.kr

Received 21 November 2019

Accepted 14 April 2020

Edited by R. W. Strange, University of Essex, UK

Keywords: X-ray free electron lasers; X-ray absorption spectroscopy; warm dense matter.

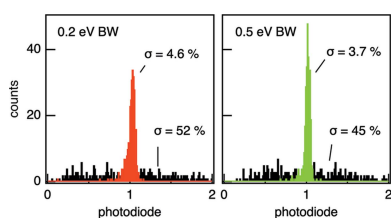
Free-electron laser pulse-based X-ray absorption spectroscopy measurements on warm dense copper are presented. The incident X-ray pulse energies were measured with a detector assembly consisting of a photocathode membrane and microchannel plates, and the transmitted energies were measured simultaneously with a photodiode detector. The precision of the absorption measurements was evaluated. For a warm dense copper foil irradiated by an intense femtosecond laser pulse, the enhanced X-ray absorption below the L_3 -edge, followed by the rapid evolution of highly excited Fermi liquid within a picosecond, were successfully measured. This result demonstrates a unique capability to study femtosecond non-equilibrium electron-hole dynamics in extreme states of matter.

1. Introduction

X-ray absorption spectroscopy (XAS) is a simple but powerful spectroscopic technique. It can provide information on local geometry, symmetries and spin configurations of element-specific electronic structures. In combination with optical lasers, it is apparent that time-resolved XAS is a powerful tool for tracking the dynamics of electronic systems (Bressler *et al.*, 2009; Volkov *et al.*, 2019) and their structures (Bressler & Chergui, 2004). Its experimental simplicity makes this technique attractive for various fields of research including material science, biology and chemistry.

Warm dense matter (WDM) is an emerging field of research between plasma and condensed matter physics. The term refers to a state of matter. It is loosely defined by a temperature of 1–10 eV and a density of 1–100 g cc⁻¹ (Lee *et al.*, 2002). Matter with both the temperature of plasma and the density of condensed matter is widespread in the universe and laboratories, for example the interior of giant planets and stars, the atmosphere of white dwarfs, laser ablation and inertial confinement fusion research (Ichimaru, 1982; Gattass & Mazur, 2008; Glenzer *et al.*, 2010; Booth *et al.*, 2015). The investigation of WDM can provide an understanding of non-equilibrium phase transitions and energy relaxation processes under extreme conditions. Owing to its high temperature and high density, however, there is a complicated interplay of physical processes. This creates significant challenges for both experimental and theoretical study.

There has been keen interest to apply a powerful time-resolved XAS technique for WDM research. In the picosecond regime, using laser plasma X-ray sources, Dorchiev *et al.* performed time-resolved X-ray absorption near-edge structure (TR-XANES) measurements near the K -edge of



warm dense aluminium heated by an intense laser pulse, and demonstrated the structural disordering from solid to gas (Dorchies *et al.*, 2011; Leguay *et al.*, 2013). Cho *et al.* used the synchrotron-based TR-XANES technique for the isochorically heated copper *L*-edge and showed that the evolution of Fermi distribution and electron–phonon coupling in WDM can be determined. (Cho *et al.*, 2011, 2016). The temporal resolutions of these measurements were of the order of picoseconds which was not fast enough to capture non-equilibrium electron–hole dynamics. In the femtosecond regime, a few measurements using laser-based short-wavelength sources have been reported. Absorption spectroscopy using high-order harmonic extreme ultraviolet and soft X-ray sources demonstrated that chemical reactions in molecules and non-equilibrium electron distributions in highly excited systems can be probed with femtosecond resolutions (Pertot *et al.*, 2017; Lee *et al.*, 2018). The betatron radiation showed possibility as a broadband femtosecond source that can be extended to the hard X-ray regime for TR-XAS measurement (Mahieu *et al.*, 2018; Kozlova *et al.*, 2020). These laser-based sources have advantages in compactness, easy accessibility and intrinsic little-to-no timing jitter between pump and probe pulses. However, for application to the broad range of elements and parameters, further developments including improved photon flux and tunability in energy and wavelength are still required.

X-ray free-electron lasers (XFELs) produce tunable, high-flux, femtosecond X-ray pulses (Emma *et al.*, 2010; Ishikawa *et al.*, 2012; Kang *et al.*, 2017). This would be ideal for ultrafast XAS measurements in WDM research. The stochastic self-amplified spontaneous emission (SASE) process and the inherently large shot-to-shot fluctuation in intensity distribution of the XFEL pulse make the application of TR-XAS at XFELs challenging (Bernstein *et al.*, 2009; Gaudin *et al.*, 2014). This problem is particularly significant for WDM applications. Owing to the high temperature and pressure of WDM, laser irradiated samples typically undergo irreversible destructive processes, and the integration of numerous X-ray pulses for quality data is hindered by slow sample refreshment. By adopting improved diagnostics and normalization techniques for SASE pulses, an XFEL transmission measurement with an accuracy of 1% or better was obtainable (Lemke *et al.*, 2013; Higley *et al.*, 2016).

In the present article, we report on the femtosecond XAS measurement of copper irradiated by an intense laser pulse at the Pohang Accelerator Laboratory X-ray Free-Electron

Laser (PAL-XFEL). The apparatus is set up at the soft X-ray scattering and spectroscopy (SSS) experimental station. The incident X-ray pulse energy measurement system consists of the photocathode membrane and microchannel plates (MCPs). Its implementation allows for proper normalization of the incident XFEL pulse energy, and for transmission through the sample to be determined with a single pulse. The precision of the X-ray absorption measurement was evaluated. For the warm dense copper sample irradiated by an intense femtosecond laser pulse, the strongly enhanced X-ray absorption below the Cu *L*₃-edge and the rapid evolution of highly excited Fermi liquid within a few picoseconds were successfully measured. This capability could give rise to opportunities for direct investigation of the femtosecond non-equilibrium electron–hole dynamics in extreme conditions of matter.

2. Experimental setup

Fig. 1 shows the schematic diagram of the TR-XAS measurement setup at the SSS experimental station of the PAL-XFEL. The soft X-ray undulator provides X-ray pulses with photon energies ranging from 250 eV to 1200 eV. Each pulse typically delivers 200 μJ of energy in less than 50 fs full width at half-maximum (FWHM) with a bandwidth of 0.44%. The maximum repetition rate is 60 Hz. A monochromator system equips two varied-line-spacing gratings (100 and 200 lines mm^{−1}) to cover the energy range 250–1200 eV. A resolution of $\Delta E/E = 1/11000$ is achieved at the exit slit. For the pump–probe measurement a Ti:sapphire laser is coupled upstream of the sample plane in the near-collinear geometry of $\sim 1^\circ$. A laser pulse can deliver up to 4 mJ of energy in 40 fs FWHM at 800 nm wavelength. The temporal jitter between the optical and X-ray pulses is less than 270 fs FWHM. More details on the general beamline equipment are described in the literature (Kang *et al.*, 2017; Park *et al.*, 2018; Kim *et al.*, 2019).

The key component is the incident X-ray pulse energy measurement system (hereafter referred to as the *I*₀ monitor). The detector assembly (Hamamatsu F2223-21SH) consists of two MCPs and a single metal anode with a central hole. The X-ray beam passes through the hole causing a secondary electron from the membrane (5 nm Pt on 200 nm Si₃N₄) located 20 mm downstream from the MCPs. A portion of electrons can be detected by the active area within a 27 mm diameter of the MCP. This assembly was also successfully

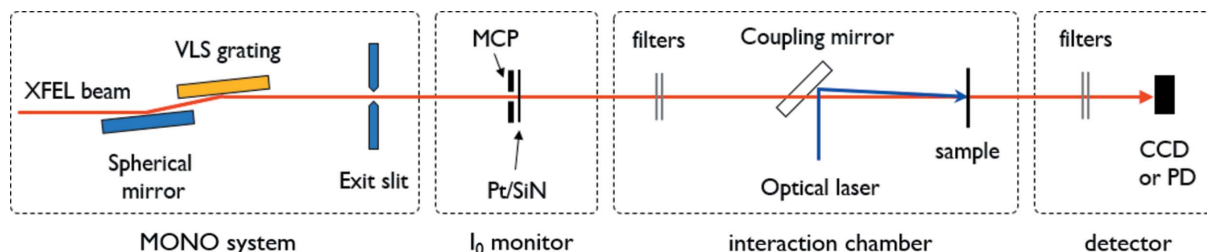


Figure 1 Schematic diagram of the time-resolved X-ray absorption spectroscopy setup at the PAL-XFEL.

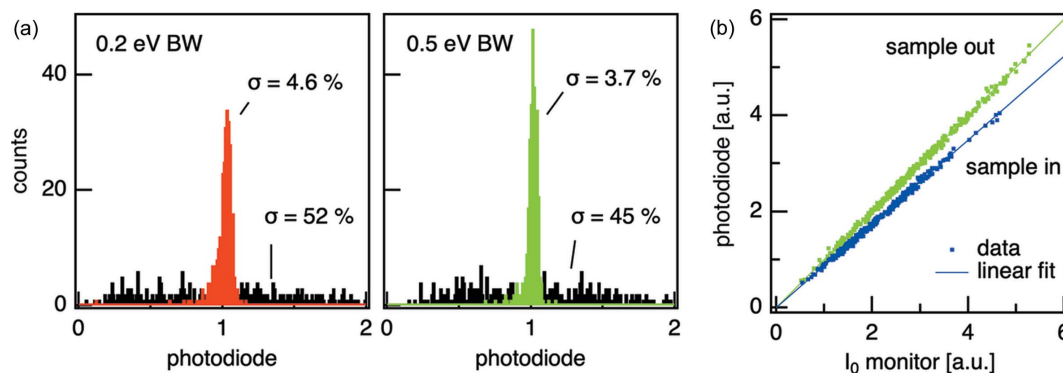


Figure 2

(a) Histograms of XFEL pulse energy after the monochromator with 0.2 eV and 0.5 eV bandwidth by photodiode (black) and by photodiode normalized by the I_0 monitor (coloured). (b) Pulse energy measured by photodiode and I_0 monitor.

commissioned at the LCLS free-electron laser (Higley *et al.*, 2016). A set of filters (10 μm Al, 20 μm Al and 400 nm Au on a 200 nm Si_3N_4 membrane) can be inserted downstream of the detector. Depending on the photon energy, these filters provide up to 10^5 attenuations. This prevents possible damage to the sample.

Transmitted X-ray pulses are detected with either an Si PIN photodiode (Hamamatsu S3590-09) or a back-illuminated charge-coupled device (CCD) (Andor iKon-L SO). The photodiode has a large active area (10 mm \times 10 mm) and high-speed response (40 MHz). The CCD is a 16-bit detector with a square sensor of 27 mm \times 27 mm active area and 2048 \times 2048 pixels. Quantum efficiency is as high as 95% at around 1000 eV. In front of the detectors, another set of metal foils (150 nm Al, 300 nm Al, 150 nm Ti and 300 nm Ti) can be inserted to block optical lights and, if needed, to provide additional attenuation of the X-rays.

Firstly, an XFEL pulse energy of 300 pulses passing through the exit slit of the monochromator was measured with only a photodiode detector. The histograms for energy distribution are shown in Fig. 2. Photodiode signals were normalized using the mean. With a bandwidth of 0.2 eV and an energy of 932 eV, a standard deviation of 52% was measured. Increasing the bandwidth to 0.5 eV reduced the standard deviation to 45%. This large fluctuation can be attributed to the noisy nature of the energy distribution in the SASE spectra. Secondly, the energy of the incident pulse is normalized with utilization of the I_0 monitor. Fig. 2(b) displays the positive correlation between the I_0 monitor and photodiode signals (sample out). Filter sets and voltage settings for the MCPs and photodiode were tuned for linearity between the two detectors. For 300 individual pulses, a linear correlation coefficient of 99.8% was obtained. When the photodiode signals were divided by the MCP signals, energy distribution histograms showed that the standard deviations were reduced to 4.6% and 3.7% for bandwidths of 0.2 eV and 0.5 eV, respectively.

For the linear correlation data in Fig. 2(b), the slope of the linear fit ($y = ax$) is the X-ray transmission, and the relative error is a standard deviation of the fitted slope which indicates the sensitivity of this measurement. Fig. 3 shows this error as a function of the number of shots, N , used for the fitting. As N

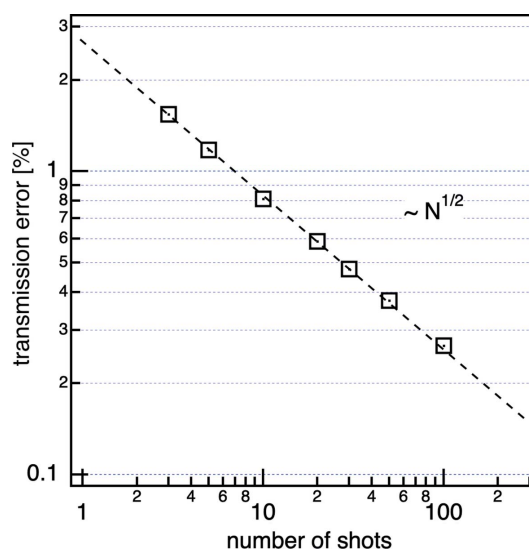


Figure 3

Transmission errors as a function of the number of shots.

increases, the transmission error reduces by $\sim N^{-1/2}$, dropping below 1% with ten shots.

3. X-ray absorption spectra of warm dense copper

Copper L_3 -edge XANES were measured using the setup described. A 40 nm free-standing copper foil (fabricated by Luxel Corporation) was used as the sample. To prevent oxidation, a 100 nm coating of SiO_2 was applied to each side of the copper foil. The addition of fine Ni mesh (70 lines per inch) prevented the distortion and ripping of the large-area (20 mm \times 20 mm) nano-foil. For proper X-ray attenuation, 10 μm Al and 150 nm Ti filters were employed in front of the sample and the detector, respectively.

Fig. 2(b) shows 300 measurements of incidence (I_0 monitor) and transmission through the copper (photodiode) (blue dots). The XFEL photon energy is 932 eV with 0.5 eV bandwidth. A linear fit shows a transmission of 0.871 ± 0.001 . The error is consistent with Fig. 3. In order to obtain a full XANES spectrum, the photon energy was scanned from 925 eV to 945 eV with increments of 0.5 eV and a 2 Hz repetition rate.

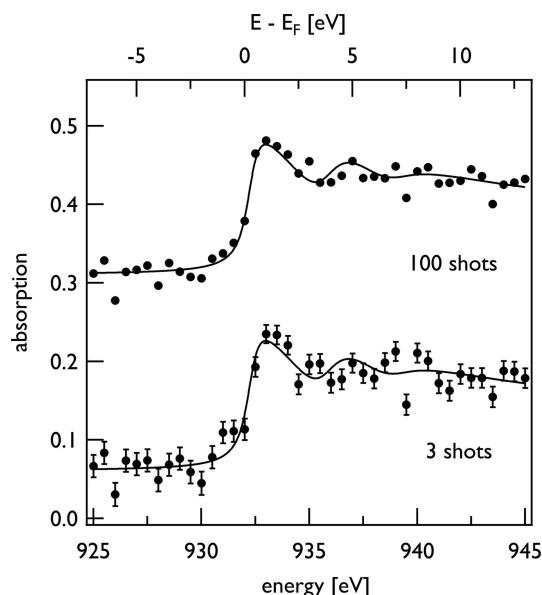


Figure 4 Cu L_3 -edge X-ray absorption spectra for 3 pulses and 100 pulses at each energy (dots). The solid line represents a reference calculation spectrum, convoluted with an experimental energy resolution.

Fig. 4 shows the measured absorption spectrum (black dots) with 3 pulses and 100 pulses averaged for each data point. The uncertainty of measurement for each data point follows the trend in Fig. 3, *i.e.* ± 0.3 and $\pm 1.5\%$ for 100 shot and 3 shot averaged data, respectively. As a reference, the spectrum obtained by density functional theory (DFT) calculation (Cho *et al.*, 2011) convoluted with the experimental resolution (0.5 eV rectangular function) is also presented (solid curves). In the 925–945 eV range, the root-mean-square deviations of the measured spectra from the reference are 1.7% and 1.2% for the 3 shot and 100 shot averaged data, respectively.

The changes caused by irradiation (by a femtosecond laser pulse) in the XAS of warm dense copper were measured. The incidence wavelength and peak fluence were 800 nm. The FWHM diameter on the sample was 150 μm and the corresponding peak fluence was $2.07 \pm 0.02 \text{ J cm}^{-2}$. The range of fluence sampled by an X-ray probe (30 $\mu\text{m} \times 60 \mu\text{m}$) was 1.85–2.07 J cm^{-2} . It was noted that sample heating was completed by the end of the laser pulse duration (40 fs). The hydrodynamic expansion of the sample

can be ignored and the initial sample density does not change. This is because the time scale of electron–phonon coupling is of the order of 10 ps. Therefore, this heating is an isochoric process, and, considering the laser energy absorbed by the sample, the corresponding electron temperature at the end of the laser pulse is as high as 1.6 eV. After each laser pulse, the sample was translated as 370 μm to avoid the damaged area. Typically, the available laser shots on a single foil are over 2500 and the repetition rate is $\sim 0.67 \text{ Hz}$.

The measured difference between warm dense and cold Cu L_3 -XANES at the selected pump–probe delays are shown in Fig. 5. For each data point, ten measurements were made. The errors in measurement were 2.0–4.0%. It is noted that these are larger than the estimated error in Fig. 3. This is due to the fluctuations in pulse energy and pointing of the optical laser, and an uncertainty in the sample thickness ($40 \pm 5 \text{ nm}$). Between 200 fs and 1400 fs after pumping, the data exhibit strong enhancement in absorption below the L_3 -edge ($E - E_F < 0$) and fast evolution. It indicates that the Cu d band, which is fully occupied under ambient conditions, becomes highly excited. This causes a significant portion of the d band to become unoccupied under the WDM condition. The distribution of unoccupied states varies rapidly in a picosecond.

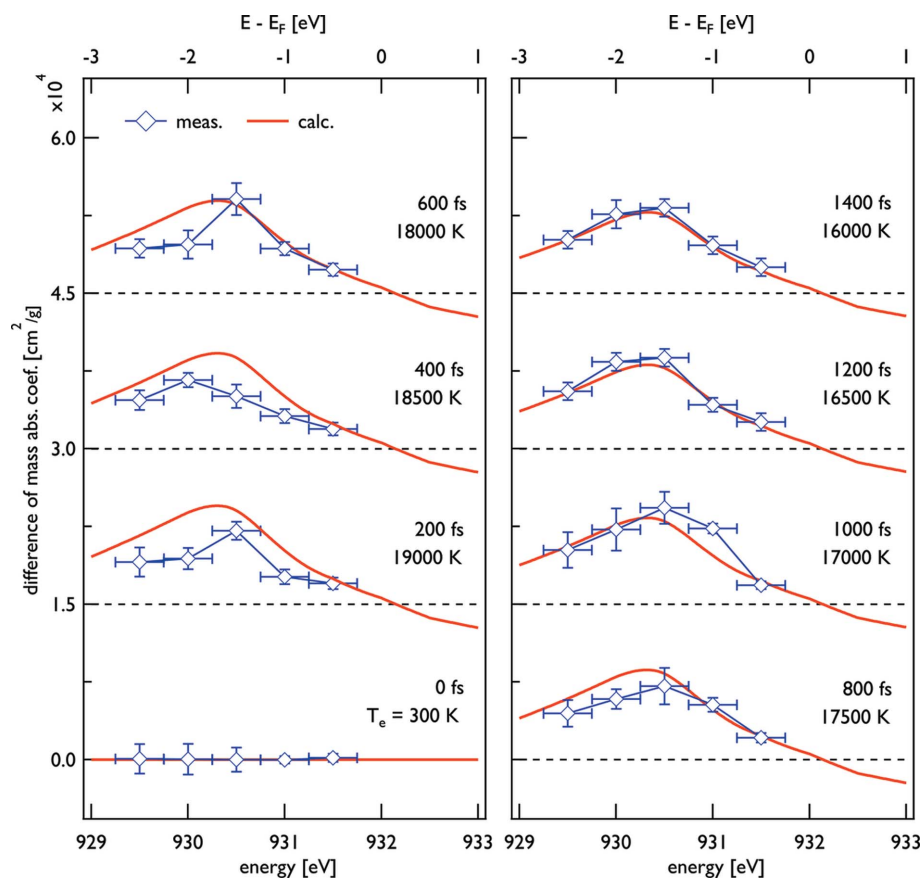


Figure 5 The measured difference between warm dense and cold XAS of copper below the Fermi level at the selected pump–probe delays (blue diamonds). For comparison, the calculated difference spectra for copper with 19000–16000 K are also shown (red curves). Spectra are displayed with an offset of 15000 along the y axis between time steps.

In the picosecond range (2–20 ps), the enhanced X-ray absorption below the L_3 -edge has been successfully explained by the Fermi distribution of electrons with a few-electronvolt temperature (Cho *et al.*, 2011, 2016). At 2 ps, the excited electronic system is already in equilibrium, and the formation of a high-temperature Fermi distribution induces unoccupied states in the $3d$ band. The decrement of electron–hole temperatures and the evolution of X-ray absorption spectra over 20 ps could be well described via enhanced electron–phonon coupling (Lin *et al.*, 2008), the two-temperature model (Anisimov *et al.*, 1974) and the corresponding XANES calculations with finite temperatures (Cho *et al.*, 2011, 2016).

We apply the same theoretical approach for the measurement in 200–1400 fs. The red curves in Fig. 5 are the differential XANES calculations assuming the Fermi-distributions with 16000–19000 K, predicted by the two-temperature model. Up to 1000 fs, significant disagreement between measurement and calculation is found. This result infers that, in the first picosecond after the laser excitation, the electrons and holes in the d band may not be in equilibrium and are hardly described by the Fermi distribution. At 1200 fs and thereafter, the measurements agree well with the calculations, and the Fermi distribution with a temperature of ~ 16000 K is established. The detailed physical interpretations of the non-equilibrium electron–hole distributions and the lifetimes of non-thermal particles are perhaps beyond the scope of this article and could be discussed in another contribution. It is emphasized that the femtosecond XANES measurement presented could provide valuable experimental insights to explore the ultrafast electron dynamics and the material properties under strong non-equilibrium conditions.

4. Conclusions

We have presented the X-ray absorption spectroscopy setup at the SSS experimental station of PAL-XFEL. Despite a large shot-to-shot fluctuation in the energy distribution of SASE spectra, the incident FEL pulse energy was properly normalized with the photocathode membrane and MCP detector, and the transmission of a monochromatic beam can be determined. Although the wide spectral range is hardly obtainable in single-shot mode with the given bandwidth (0.44%) of FEL pulse, the quality of the spectra presented and the measurement sensitivity with a small number of shots provided crucial advantages for scanning large parameter space in destructive samples. In particular, the pump–probe measurement for copper foil demonstrated its ability to capture femtosecond non-equilibrium electron–hole dynamics under WDM conditions. This will be an essential experimental capability for further understanding of energy transport, phase transitions and material properties in the extreme state of matter.

Acknowledgements

The technical support from the PAL-XFEL accelerator and beamline divisions is gratefully acknowledged.

Funding information

This work has been supported by the Institute for Basic Science (grant No. IBS-R012-D1) and the National Research Foundation of Korea (grant Nos. NRF-2015R1A5A1009962; NRF-2019R1A2C2002864; NRF-2019K2A9A2A08000160; NRF-2018R1D1A1B07046676).

References

- Anisimov, S., Kapeliovich, B. & Perelman, T. (1974). *Zh. Eksp. Teor. Fiz.* **66**, 375–377.
- Bernstein, D. P., Acremann, Y., Scherz, A., Burkhardt, M., Stöhr, J., Beye, M., Schlotter, W. F., Beeck, T., Sorgenfrei, F., Pietzsch, A., Wurth, W. & Föhlisch, A. (2009). *Appl. Phys. Lett.* **95**, 134102.
- Booth, N., Robinson, A. P. L., Hakel, P., Clarke, R. J., Dance, R. J., Doria, D., Gizzi, L. A., Gregori, G., Koester, P., Labate, L., Levato, T., Li, B., Makita, M., Mancini, R. C., Pasley, J., Rajeev, P. P., Riley, D., Wagenaars, E., Waugh, J. N. & Woolsey, N. C. (2015). *Nat. Commun.* **6**, 8742.
- Bressler, C. & Chergui, M. (2004). *Chem. Rev.* **104**, 1781–1812.
- Bressler, C., Milne, C., Pham, V.-T., Elnahhas, A., van der Veen, R. M., Gawelda, W., Johnson, S., Beaud, P., Grolimund, D., Kaiser, M., Borca, C. N., Ingold, G., Abela, R. & Chergui, M. (2009). *Science*, **323**, 489–492.
- Cho, B. I., Engelhorn, K., Correa, A. A., Ogitsu, T., Weber, C. P., Lee, H. J., Feng, J., Ni, P. A., Ping, Y., Nelson, A. J., Prendergast, D., Lee, R. W., Falcone, R. W. & Heimann, P. A. (2011). *Phys. Rev. Lett.* **106**, 167601.
- Cho, B. I., Ogitsu, T., Engelhorn, K., Correa, A. A., Ping, Y., Lee, J. W., Bae, L. J., Prendergast, D., Falcone, R. W. & Heimann, P. A. (2016). *Sci. Rep.* **6**, 18843.
- Dorchies, F., Lévy, A., Goyon, C., Combis, P., Descamps, D., Fourment, C., Harmand, M., Hulin, S., Leguay, P. M., Petit, S., Peyrusse, O. & Santos, J. J. (2011). *Phys. Rev. Lett.* **107**, 245006.
- Emma, P., Akre, R., Arthur, J., Bionta, R., Bostedt, C., Bozek, J., Brachmann, A., Bucksbaum, P., Coffee, R., Decker, F. J., Ding, Y., Dowell, D., Edstrom, S., Fisher, A., Frisch, J., Gilevich, S., Hastings, J., Hays, G., Hering, P., Huang, Z., Iverson, R., Loos, H., Messerschmidt, M., Miahnahri, A., Moeller, S., Nuhn, H. D., Pile, G., Ratner, D., Rzepiela, J., Schultz, D., Smith, T., Stefan, P., Tompkins, H., Turner, J., Welch, J., White, W., Wu, J., Yocky, G. & Galayda, J. (2010). *Nat. Photon.* **4**, 641.
- Gattass, R. R. & Mazur, E. (2008). *Nat. Photon.* **2**, 219.
- Gaudin, J., Fourment, C., Cho, B. I., Engelhorn, K., Galtier, E., Harmand, M., Leguay, P. M., Lee, H. J., Nagler, B., Nakatsutsumi, M., Ozkan, C., Störmer, M., Toleikis, S., Tschentscher, T., Heimann, P. A. & Dorchies, F. (2014). *Sci. Rep.* **4**, 4724.
- Glenzer, S. H., MacGowan, B. J., Michel, P., Meezan, N. B., Suter, L. J., Dixit, S. N., Kline, J. L., Kyrala, G. A., Bradley, D. K., Callahan, D. A., Dewald, E. L., Divol, L., Dzenitis, E., Edwards, M. J., Hamza, A. V., Haynam, C. A., Hinkel, D. E., Kalantar, D. H., Kilkenny, J. D., Landen, O. L., Lindl, J. D., LePape, S., Moody, J. D., Nikroo, A., Parham, T., Schneider, M. B., Town, R. P. J., Wegner, P., Widmann, K., Whitman, P., Young, B. K. F., Van Wousterghem, B., Atherton, L. J. & Moses, E. I. (2010). *Science*, **327**, 1228–1231.
- Higley, D. J., Hirsch, K., Dakovski, G. L., Jal, E., Yuan, E., Liu, T., Lutman, A. A., MacArthur, J. P., Arenholz, E., Chen, Z., Coslovich, G., Denes, P., Granitzka, P. W., Hart, P., Hoffmann, M. C., Joseph, J., Le Guyader, L., Mitra, A., Moeller, S., Ohldag, H., Seaberg, M., Shafer, P., Stöhr, J., Tsukamoto, A., Nuhn, H. D., Reid, A. H., Dürr, H. A. & Schlotter, W. F. (2016). *Rev. Sci. Instrum.* **87**, 033110.
- Ichimaru, S. (1982). *Rev. Mod. Phys.* **54**, 1017–1059.
- Ishikawa, T., Aoyagi, H., Asaka, T., Asano, Y., Azumi, N., Bizen, T., Ego, H., Fukami, K., Fukui, T., Furukawa, Y., Goto, S., Hanaki, H.,

- Hara, T., Hasegawa, T., Hatsui, T., Higashiya, A., Hirono, T., Hosoda, N., Ishii, M., Inagaki, T., Inubushi, Y., Itoga, T., Joti, Y., Kago, M., Kameshima, T., Kimura, H., Kiriwara, Y., Kiyomichi, A., Kobayashi, T., Kondo, C., Kudo, T., Maesaka, H., Maréchal, X. M., Masuda, T., Matsubara, S., Matsumoto, T., Matsushita, T., Matsui, S., Nagasono, M., Nariyama, N., Ohashi, H., Ohata, T., Ohshima, T., Ono, S., Otake, Y., Saji, C., Sakurai, T., Sato, T., Sawada, K., Seike, T., Shirasawa, K., Sugimoto, T., Suzuki, S., Takahashi, S., Takebe, H., Takeshita, K., Tamasaku, K., Tanaka, H., Tanaka, R., Tanaka, T., Togashi, T., Togawa, K., Tokuhisa, A., Tomizawa, H., Tono, K., Wu, S., Yabashi, M., Yamaga, M., Yamashita, A., Yanagida, K., Zhang, C., Shintake, T., Kitamura, H. & Kumagai, N. (2012). *Nat. Photon.* **6**, 540–544.
- Kang, H.-S., Min, C.-K., Heo, H., Kim, C., Yang, H., Kim, G., Nam, I., Baek, S. Y., Choi, H.-J., Mun, G., Park, B. R., Suh, Y. J., Shin, D. C., Hu, J., Hong, J., Jung, S., Kim, S.-H., Kim, K., Na, D., Park, S. S., Park, Y. J., Han, J.-H., Jung, Y. G., Jeong, S. H., Lee, H. G., Lee, S., Lee, W.-W., Oh, B., Suh, H. S., Parc, Y. W., Park, S.-J., Kim, M. H., Jung, N.-S., Kim, Y.-C., Lee, M.-S., Lee, B.-H., Sung, C.-W., Mok, I.-S., Yang, J.-M., Lee, C.-S., Shin, H., Kim, J. H., Kim, Y., Lee, J. H., Park, S.-Y., Kim, J., Park, J., Eom, I., Rah, S., Kim, S., Nam, K. H., Park, J., Park, J., Kim, S., Kwon, S., Park, S. H., Kim, K. S., Hyun, H., Kim, S. N., Kim, S., Hwang, S., Kim, M. J., Lim, C., Yu, C.-J., Kim, B.-S., Kang, T.-H., Kim, K.-W., Kim, S.-H., Lee, H.-S., Lee, H.-S., Park, K.-H., Koo, T.-Y., Kim, D.-E. & Ko, I. S. (2017b). *Nat. Photon.* **11**, 708–713.
- Kim, M., Min, C.-K. & Eom, I. (2019). *J. Synchrotron Rad.* **26**, 868–873.
- Kozlova, M., Andriyash, I., Gautier, J., Sebban, S., Smartsev, S., Jourdain, N., Chulagain, U., Azamoum, Y., Tafzi, A., Goddet, J.-P., Oubrierie, K., Thauray, C., Rousse, A. & Ta Phuoc, K. (2020). *Phys. Rev. X*, **10**, 011061.
- Lee, J.-W., Geng, X., Jung, J. H., Cho, M. S., Yang, S. H., Jo, J., Lee, C., Cho, B. I. & Kim, D. (2018). *Nucl. Instrum. Methods Phys. Res. A*, **895**, 120–125.
- Lee, R. W., Baldis, H. A., Cauble, R. C., Landen, O. L., Wark, J. S., Ng, A., Rose, S. J., Lewis, C., Riley, D., Gauthier, J. C. & Audebert, P. (2002). *Laser Part. Beams*, **20**, 527–536.
- Leguay, P. M., Lévy, A., Chimier, B., Deneuveville, F., Descamps, D., Fourment, C., Goyon, C., Hulin, S., Petit, S., Peyrusse, O., Santos, J. J., Combis, P., Holst, B., Recoules, V., Renaudin, P., Videau, L. & Dorchies, F. (2013). *Phys. Rev. Lett.* **111**, 245004.
- Lenke, H. T., Bressler, C., Chen, L. X., Fritz, D. M., Gaffney, K. J., Galler, A., Gawelda, W., Haldrup, K., Hartsock, R. W., Ihee, H., Kim, J., Kim, K. H., Lee, J. H., Nielsen, M. M., Stickrath, A. B., Zhang, W., Zhu, D. & Cammarata, M. (2013). *J. Phys. Chem. A*, **117**, 735–740.
- Lin, Z., Zhigilei, L. V. & Celli, V. (2008). *Phys. Rev. B*, **77**, 075133.
- Mahieu, B., Jourdain, N., Ta Phuoc, K., Dorchies, F., Goddet, J. P., Lifschitz, A., Renaudin, P. & Lecherbourg, L. (2018). *Nat. Commun.* **9**, 3276.
- Park, S. H., Kim, M., Min, C.-K., Eom, I., Nam, I., Lee, H.-S., Kang, H.-S., Kim, H.-D., Jang, H. Y., Kim, S., Hwang, S., Park, G. S., Park, J., Koo, T. Y. & Kwon, S. (2018). *Rev. Sci. Instrum.* **89**, 055105.
- Pertot, Y., Schmidt, C., Matthews, M., Chauvet, A., Huppert, M., Svoboda, V., von Conta, A., Tehlar, A., Baykusheva, D., Wolf, J.-P. & Wörner, H. J. (2017). *Science*, **355**, 264–267.
- Volkov, M., Sato, S. A., Schlaepfer, F., Kasmi, L., Hartmann, N., Lucchini, M., Gallmann, L., Rubio, A. & Keller, U. (2019). *Nat. Phys.* **15**, 1145–1149.